Environmental Science & Technology

Article

Cite This: *Environ. Sci. Technol.* 2019, 53, 5230−5240

pubs.acs.org/est

In Situ Intermediates Determination and Cytotoxicological Assessment in Catalytic Oxidation of Formaldehyde: Implications for Catalyst Design and Selectivity Enhancement under Ambient Conditions

Haiwei Li,[†] Long Cui,[†,‡] Yanfeng Lu,[‡] Yu Huang,[‡] Junji Cao,[‡] Duckshin Park,[§] Shun-cheng Lee,[*,†] and Wingkei Ho[*,∥,∥∥]

[†]Department of Civil and Environmental Engineering, The Hong Kong Polytechnic University, Hong Kong, China

[‡]State Key Laboratory of Loess and Quaternary Geology (SKLLQG) and Key Laboratory of Aerosol Chemistry and Physics, Institute of Earth Environment, Chinese Academy of Sciences, Xi'an 710061, China

[§]Transportation Environmental Research Team, The Korea Railroad Research Institute, Gyeonggi-do, South Korea

[∥]Department of Science and Environmental Studies, The Education University of Hong Kong, Hong Kong, China

[∥∥]State Key Laboratory of Marine Pollution, The City University of Hong Kong, Hong Kong, China

Supporting Information

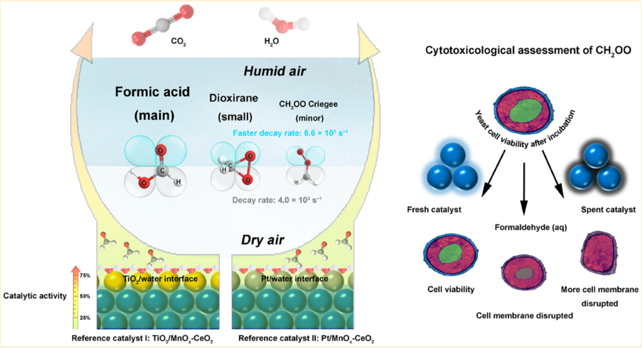

ABSTRACT: Formation and decay of formaldehyde oxides (CH_2OO) affect the complete oxidation of formaldehyde. However, the speciation and reactivity of CH_2OO are poorly understood because of its extremely fast kinetics and indirect measurements. Herein, three isomers of CH_2OO (i.e., main formic acid, small dioxirane, and minor CH_2OO Criegee) were in situ determined and confirmed as primary intermediates of the room-temperature catalytic oxidation of formaldehyde with two reference catalysts, that is, TiO_2/MnO_x-CeO_2 and Pt/MnO_x-CeO_2. CH_2OO Criegee is quite reactive, whereas formic acid and dioxirane have longer lifetimes. The production, stabilization, and removal of the three intermediates are preferentially performed at high humidity, matching well with the decay rate of CH_2OO at approximately 6.6×10^3 s^{-1} in humid feed gas faster than 4.0×10^3 s^{-1} in dry feed. By contrast, given that a thinner water/TiO_2 interface was well-defined in TiO_2/MnO_x-CeO_2, fewer reductions in the active sites and catalytic activity were found when humidity was decreased. Furthermore, lethal intermediates mostly captured at the TiO_2/MnO_x-CeO_2 surface suppressed the toxic off-gas emissions. This study provides practical insights into the rational design and selectivity enhancement of a reliable catalytic process for indoor air purification under unfavorable ambient conditions.

INTRODUCTION

Formaldehyde oxides (CH_2OO), the simplest carbonyl oxides or Criegee intermediates, have been recognized as important transient intermediates in tropospheric oxidation[1−5] but have been rarely studied in the catalytic oxidation of formaldehyde (CH_2O). A large fraction of CH_2OO in the atmosphere, whose longest lifespan is 0.05−2 ms[2,6], incur extremely reactive bimolecular reactions with species such as trace gases (e.g., SO_2 and NO),[2] peroxy radical and organic acid,[3,4,7] and water vapor.[5] Only few reports[2,4,5] on direct measurements of CH_2OO are available. CH_2OO Criegee and its isomers (i.e., formic acid and dioxirane)[6,8] are identified through vacuum-ultraviolet photoionization mass spectrometry in a chamber simulation of CH_2I_2/O_2 photolysis.[2,4] The decay rate of CH_2OO reaction with water vapor at high relative humidity (RH = 85%) is much faster than that with CH_2OO scavengers, such as SO_2 and NO_2, in a relatively dry atmosphere (RH = 35%).[5,9]

However, whether the CH_2OO chemistry is similar in the catalytic oxidation of CH_2O remains to be elucidated. Room-temperature catalytic oxidation (RCO) using either transition metal-based catalysts or noble metal-based catalysts has become an energetically attractive approach to reduce CH_2O in indoor air.[10−15] Given the diurnal or regional variations in ambient temperature and humidity, the RCO of CH_2O is limited by the moisture-dependent activity at low temperatures.[16−18] Our group has thus focused on the surface

Received: November 18, 2018
Revised: April 15, 2019
Accepted: April 16, 2019
Published: April 16, 2019

ACS Publications

DOI: 10.1021/acs.est.8b06234

hydrophilic modification of RCO catalysts. With the capability of active-site exposure and activation of reactive oxygen species at low temperatures, the MnO_x-CeO_2 catalyst (MCO) is often modified by other catalysts or elements in hybrid fabrications.[19−21] Accordingly, MCO-supported colloidal TiO_2 catalyst[22] was synthesized to form a water/TiO_2 interface,[23−25] resulting in approximately 41% (dry air) of recycling activity compared with 57% in high humidity at room temperature. To date, making direct measurements of CH_2OO intermediates during CH_2O oxidation is challenging, and such intermediates are roughly estimated by the proposed bridging modes of carboxylic groups.[16,17,26] Two primary CH_2OO intermediates, that is, formic acid (10.82 eV) and dioxirane (11.33 eV), were preliminarily identified at different photoionization energies by in situ time-of-flight photoionization mass spectrometry. The formation of the two intermediates favors moisture as supported by evidence of the hydroxymethyl hydroperoxide ($HOCH_2OOH$, HMHP) yield from the reaction of CH_2OO with water vapor.[2,22,27] These findings help elucidate the complete reaction pathways of CH_2O oxidation. Nevertheless, the production, stabilization, and removal of CH_2OO have not been fully studied. Moreover, although the toxicity of formaldehyde is well reported, the potential environmental impacts from the released CH_2OO intermediates remain unknown.[28−30]

Herein, in situ determinations of the CH_2OO speciation and kinetics during the RCO of CH_2O were investigated through vacuum-ultraviolet time-of-flight photoionization mass spectrometry. A distinct hydrophilic structure was observed in the surface chemistry of water interacting with TiO_2[23,24,31] and Pt.[32,33] Two different MnO_x-CeO_2-based catalysts, namely MnO_x-CeO_2-supported TiO_2 and MnO_x-CeO_2-supported Pt (denoted as TO/MCO and Pt/MCO, respectively), were modified and characterized after the loading treatment was administered to attain the interfacial hydration structure. Compared with that in Pt/MCO, a thinner ordered interface between molecular water and TiO_2 surface was found in TO/MCO. As such, the adsorption and complete oxidation of CH_2O to CO_2 were compared and examined in humid and dry feeds. After the reaction was terminated toward yeast cells, a cytotoxicological study of the spent catalysts was conducted to further evaluate the inhibition of toxic intermediate emissions relative to the cytotoxicity of fresh catalysts and formaldehyde.

■ MATERIALS AND METHODS

Catalyst Synthesis. The preparations of the precursor MCO and TO/MCO are described in the Supporting Information (SI). Pt/MCO was prepared via a wet impregnation route. In brief, 500 mg of the as-prepared MCO was added dropwise to a mixture containing 30 mL of ultrapure water (Milli-Q system, Millipore Inc.), and 5 mL of H_2PtCl_6 (2 $mg\cdot mL^{-1}$) aqueous solution was achieved under stirring. After impregnation for 30 min, 10 mL of the mixed solution of $NaBH_4$ (0.1 $mol\cdot L^{-1}$) and NaOH (0.5 $mol\cdot L^{-1}$) was rapidly injected into the suspension until uniform contact with the whole surface of the suspension was achieved under stirring. The molar ratio of Pt:$NaBH_4$:NaOH was approximated to 1:5:25. After reduction for 30 min, the final suspension was washed and centrifugated with ultrapure water five times and dried in an oven at 65 °C for 6 h. The mass ratio of Pt to MCO was determined to be 1.8% (SI Table S1).

Characterizations. X-ray powder diffraction (XRD) of the as-prepared catalysts was performed using Philips X'pert Pro Super diffractometer with Cu Kα radiation (λ = 0.15406 nm). The micromorphology of the catalysts was observed under a JEOL JEM-2010 transmission electron microscope (TEM). The Brunauer−Emmett−Teller (BET) surface area was obtained by N_2 adsorption/desorption isotherms at 77 K on a Micromeritics Gemini VII 2390 instrument. Elemental contents were precisely determined by inductively coupled plasma atomic emission spectroscopy on a Vista MPX ICP system (Varian). X-ray photoemission spectroscopy (XPS) was performed on a Thermo ESCALAB 250 system, and all of the binding energies were calibrated to the C 1s peak at 284.8 eV of the surface adventitious carbon. Pyridine adsorbed IR spectroscopy (Py-IR) was conducted with Fourier transform infrared (FT−IR; Tensor 27, Bruker, Germany) spectrometer equipped with an in situ vacuum (10^{-3} Pa) IR cell reactor. The sample was purged with pure He gas at a heating rate of 10 $°C\cdot min^{-1}$ to 400 °C and then cooled to room temperature in the vacuum cell. Pyridine vapor was in situ introduced until the adsorbed pyridine approached saturation. Desorption of the adsorbed sample was conducted at a similar heating rate of 10 $°C\cdot min^{-1}$ to 450 °C. The Py-IR spectra were obtained with a resolution of 4 cm^{-1} (32 scans). The OH stretching region (2800−3800 cm^{-1}) at the surface of catalysts was characterized by sum frequency generation (SFG) spectroscopy (SI Figure S1).

In Situ C 1s XPS Analysis. In situ XPS studies were investigated using a Vacuum Generators Escalab 220 XL spectrometer equipped with monochromatized aluminum X-ray irradiation (Al Kα = 1486.6 eV) and an in situ cell reactor. The CH_2O-saturated sample was preheated from 25 to 175 °C under an Ar feed gas at a rate of 2 $°C\cdot min^{-1}$. The sample was cooled under the Ar feed gas to 25 °C after the required temperature was reached, and in situ XPS analysis was performed in the cell reactor. The C 1s XP spectra were fitted by a peak-fitting program with a mixed Gaussian (70%)/Lorentzian (30%) peak shape.

Catalytic Activity Test. Catalytic oxidation of CH_2O was conducted in a thermostatic fixed-bed reaction system. Gaseous CH_2O was diluted with a carrier gas (5 ppm of CH_2O/21% O_2/N_2 balance, RH = 0.7%−90%, GHSV = 6 × 10^4 h^{-1}). Then, 0.15 $L\cdot min^{-1}$ of the gas flow rate and 5 ppm of inlet CH_2O concentrations were stoichiometrically determined by a mass flow controller (Brooks 5860E). Afterward, 50 mg of test catalysts sieved between 40 and 60 mesh was loaded on silica wool in a stainless-steel thermocouple tube (8 mm diameter) of the fixed-bed reactor. The RH during the reaction was controlled by adjusting the ratio of humid air in the carrier gas, and the temperature was controlled with T-measuring thermocouples inside the stainless-steel tube. The outlet concentrations of CH_2O and CO_2 were monitored with a photoacoustic multigas monitor (model 1412i, LumaSense INNOVA Technologies Inc., Denmark). The error bars (standard deviation) in the activity tests were calculated from repeat measurements.

In Situ Measurements of CH_2OO. CH_2OO speciation and kinetics were directly determined through vacuum-ultraviolet time-of-flight photoionization mass spectrometry. A schematic of the experimental setup is given in SI Figure S2.

Confocal Microscopy of Spent Nanoparticles (NPs) toward Yeast Cells. Yeast (*Saccharomyces cerevisiae*, JCM 7255) was incubated with agitation at 30 °C in a yeast extract

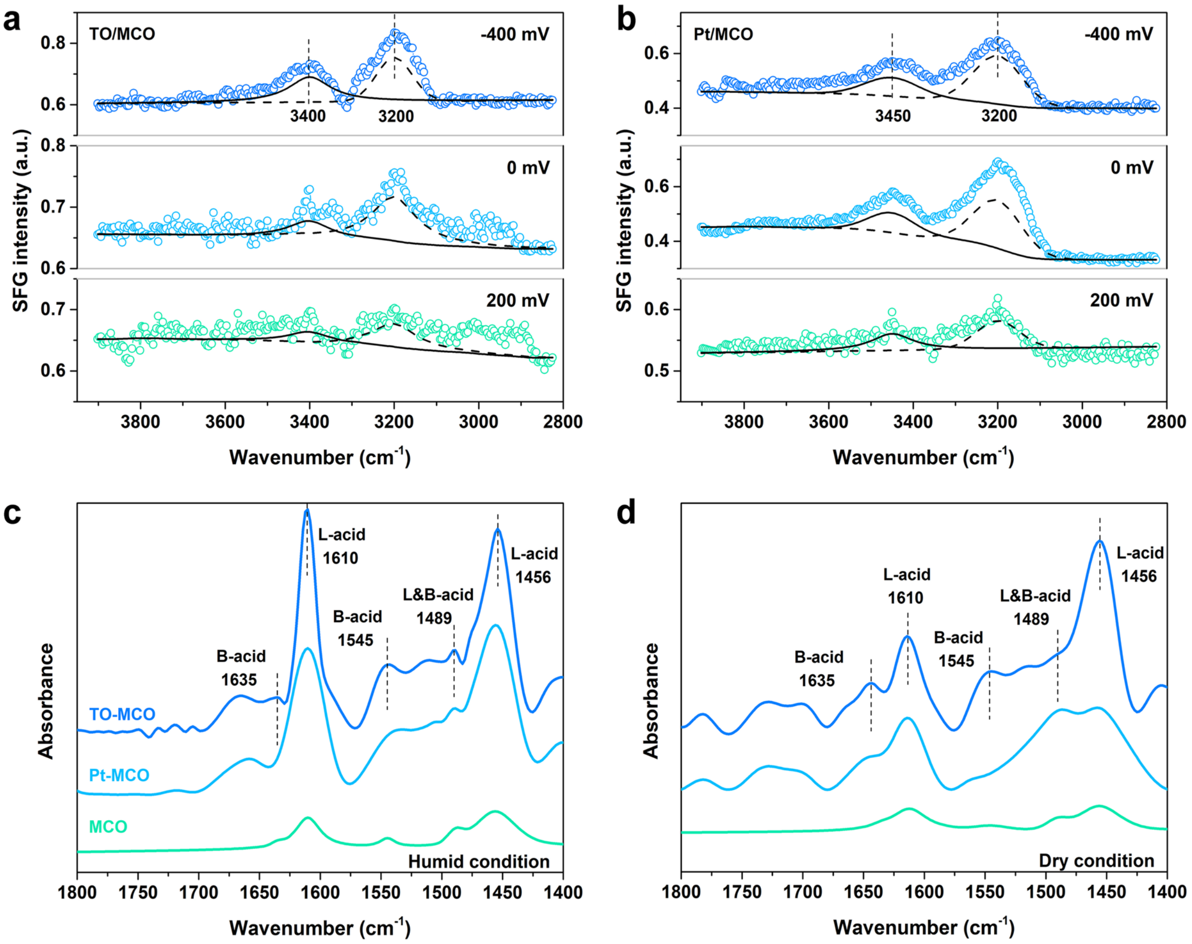

Figure 1. Potential dependence of the SFG spectra in the OH stretching region (2800−3800 cm^{-1}) at the surface of TO/MCO (a) and Pt/MCO (b) electrodes in a 0.1 M $HClO_4$ electrolyte solution. SFG spectra were fitted by two broad OH bands centered at low (dash line) and high (solid line) wavenumbers. Py-IR measurements of active sites over TO/MCO and Pt/MCO under humid (c) and dry (d) conditions.

(YE) medium (5.0 g·L^{-1} YE and 30 g·L^{-1} glucose). After the yeast suspension was centrifugated at 8000*g* at 3 °C for 10 min, the harvested yeast cells in the late exponential growth phase were washed thrice with the sterilized NaCl aqueous solution (5 mM). NaCl aqueous solution was also used as the dispersion medium.

The NPs were subjected to toxicity tests. Prior to cell exposure, the spent NPs were sealed instantly in storage at 3 °C when the CH_2O-exposed reaction was terminated. The yeast suspension with an initial concentration of 1 × 10^6 cells·mL^{-1} was exposed to 5 mM aqueous NaCl solution in a sterilized microtube containing different concentrations of NP suspension (0.5, 5, 10, 25, 50, and 100 μg·mL^{-1}). Next, the microtube was placed on a Duck rotor at 60 rpm for 1 h at 30 °C. The mixture suspension was spread on YE agar plates for 1 h incubation at 30 °C. The cell suspension without NPs on a YE agar (2.0% (w/v)) plate was tested as a control group. Toxicity was evaluated by counting the colony-forming units (CFUs) of living cells given in the fluorescence image using fluorescence cellular scanning microscopy (FCSM) with a 488 nm laser for excitation (Olympus laser-based point scanning FV-1000D confocal fluorescent microscope). Cell viability was compared by staining the combination of two membrane-permeable dyes: propidium iodide (PI) and 4′,6-diamidino-2-phenylindole (DAPI). PI only infiltrates cells with a disrupted membrane, whereas DAPI can enter all cells. In the fluorescence images, live cells were labeled with a green fluorophore, whereas disrupted or dead cells were marked with a purple fluorophore.

RESULTS AND DISCUSSION

Assembly of Hydrophilic Interface Favorable to Active-Site Exposure. Exploring a water/metal oxide interface of RCO catalysts is crucial to their practical applications in CH_2O removal at unfavorable reaction temperatures and moistures. Aside from the enlarged specific surface area and pore volume (SI Table S1), the surface modifications with TiO_2 and Pt loading, which exhibit an ordered array of the hydrophilic interfacial structure at the vicinity of their surfaces,[17,22,23,32,34] are examined to improve CH_2O adsorption and catalytic oxidation. First, the crystal structure and morphology of TO/MCO and Pt/MCO are illustrated in SI Figures S3 and S4, respectively. TO/MCO shows approximately 5 nm thin loading of TiO_2 with a uniformly exposed anatase facet (101) on the MCO surface, whereas a small size distribution (approximately 2.4 nm) of Pt NPs for Pt/MCO retains the unchanged morphology, particle size, and exposed facets of the precursor MCO.

The structural arrangement of water molecules at TO/MCO and Pt/MCO was characterized through SFG spectroscopy[32,33] in an internal reflection mode as a function of the energy of infrared radiation (IR). The SFG spectra in the

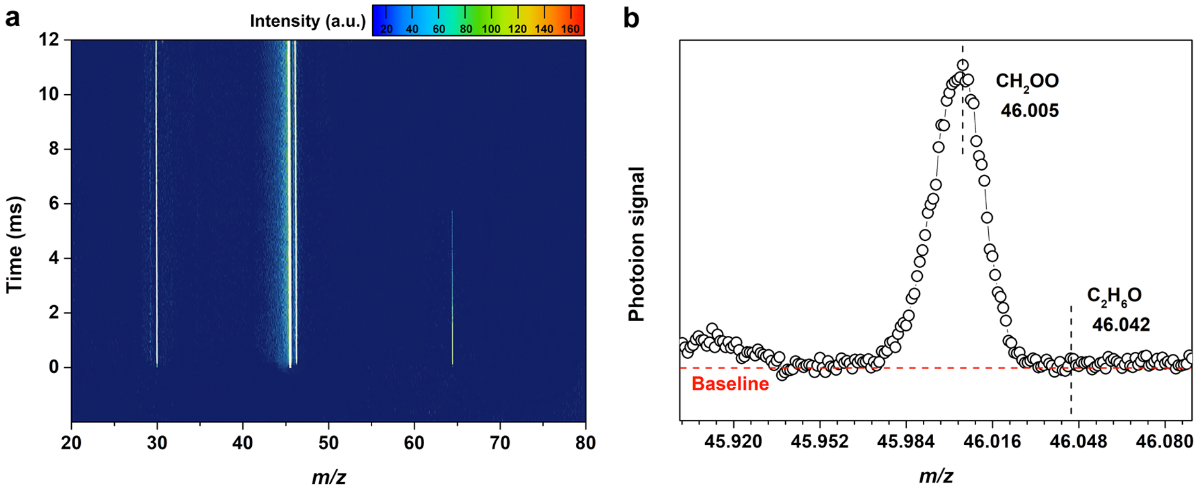

Figure 2. Time-resolved photoionization mass spectra of the CH_2OO signal during the catalytic oxidation of CH_2O (a). Time-of-flight distribution of the $m/z = 46$ photoion signal (b).

hydroxyl molecule (OH) stretching vibration region were generally featured by two broad peaks at ca. 3200 and 3400 cm^{-1}. These peaks are assigned to the symmetric OH stretching of water molecules (i.e., strongly hydrogen bonded "ice-like" water structure) and the asymmetric OH stretching in a more random arrangement (i.e., less ordered "liquid-like" water), respectively.[33] In Figure 1a and b, two broad peaks for Pt/MCO were observed in the OH stretching region (2800−3800 cm^{-1}) at ca. 3200 and 3450 cm^{-1}. By contrast, two broad OH bands for TO/MCO were centered at ca. 3200 cm^{-1} and at a slightly low wavenumber at ca. 3400 cm^{-1}. On the basis of the IR study of water clusters, the SFG spectra prove that the highly ordered "ice-like" interfacial water molecules were distributed at the vicinity of the clean surface of TO/MCO and Pt/MCO. The potential dependence of interfacial water at TO/MCO and Pt/MCO was also investigated. The SFG spectra of OH bands, which were fitted as the equation of SFG intensity (SI eq S1), can be considered an index of the order of interfacial water and varies as surface oxide is formed. The SFG intensity weakened after the maximum was reached at zero potential in the Pt/MCO electrode when the potential changes from positive (200 mV) to negative (−400 mV). Conversely, the intensity sharply increased as the potential in the TO/MCO electrode was decreased. The charge of the TO/MCO surface was higher than that of Pt/MCO (SI Figure S5). Accordingly, oxygen-up and oxygen-down orientations were stimulated on negatively and positively charged surfaces, respectively. Consequently, the ordered water layer at the vicinity of the TO/MCO surface became thin. CH_2O adsorption, which is initiated by the hydroxyl bonding of water molecules with the methyl groups of formaldehyde and formate intermediates,[35] is feasible at this interfacial hydrophilic structure even in dry atmosphere.

Next, the effects of moisture on surface active-site behaviors were investigated through Py-IR measurements.[36] Two kinds of surface metal sites, namely, Lewis acid (L-acid) and Brønsted acid (B-acid) sites, are discussed due to free electron and proton exchange at metallic catalysts. The L-acid−base properties of the metal oxides, ascribed to the cyclic electron transfer, have important implications for the oxidation selectivity and activation of reactive oxygen of catalysts.[22,37−39] In Figure 1c and d, the peaks at ca. 1456 and 1610 cm^{-1} bands were related to pyridine adsorbed onto L-acid sites, and the peaks at approximately ca. 1545 and 1635 cm^{-1} bands were assigned to B-acid sites. The peak at ca. 1489 cm^{-1} originated from pyridine adsorbed onto L-acid and B-acid sites, and the peak at ca.1474 cm^{-1} was assigned to the C−H exchange or hopping of hydrocarbon compounds to oxygen atoms.[36,37] Compared with Pt/MCO under humid conditions, TO/MCO shows a high degree of nucleophilic substitution (an exchange of metal sites (M) with oxygen atoms (O), namely the formation of M−O structure), where the Brønsted/Lewis (B/L) ratio at TO/MCO was 0.51 lower than that at Pt/MCO with 0.64. In the dry feed, TO/MCO maintained sufficient exposure of the L-acid site with a B/L ratio of 0.67, whereas an apparent decrease in L-acid sites was found at Pt/MCO with a B/L ratio of 0.80. L-acid sites are restricted if ion exchanges appear between metal ions and protons,[36] and Brønsted acid sites act as predominant active sites at high temperatures (>200 °C).[37,40] Molecular water at the vicinity of metal oxides induces a proton transfer to form a water dimer with the hydroxyl overlayer,[23,36] which comprises $H_5O_2^+$. Numerous L-acid sites were found at TO/MCO in humid air possibly because of the formation of the water dimer. Hence, the effect of a water dimer on the as-generated porous water layer of TO/MCO is substantial, leading to the predominance of L-acid sites. These events can facilitate the activation of surface oxygen species into reactive oxygen species, which was induced by cyclic electron transfer at the active sites in metallic dismutation reactions.[22]

High-resolution XPS spectra (SI Figure S6) were obtained to study the ion exchange at TO/MCO and Pt/MCO before and after the reaction and further verify the effects of moisture on the active-site behaviors. High oxidation states of Mn were maintained in fresh TO/MCO and Pt/MCO (SI Figure S7). After the reaction was terminated, the increased proportions of surface Mn^{4+}/Mn^{3+} ranged from 2.73 to 3.27 at TO/MCO. Some losses of surface oxygen species occurred at TO/MCO throughout the dismutation reactions, in which the ratios of surface lattice oxygen (O_{latt}) to surface adsorbed oxygen (O_{ads}) remained at 0.34−0.36. Ti−O depositions on O-defect sites of MnO_x−CeO_2[22,41,42] remediated the participation of oxygen species in TO/MCO (see the intense O 1s XPS signal in SI Figure S3b). Selective electron transfers from Ce^{4+} to Mn^{3+} enhanced the charge storage of the neighboring MnO_x in the bimetallic (Mn−Ce) dismutation system.[22] Hence, a few Ce^{4+}

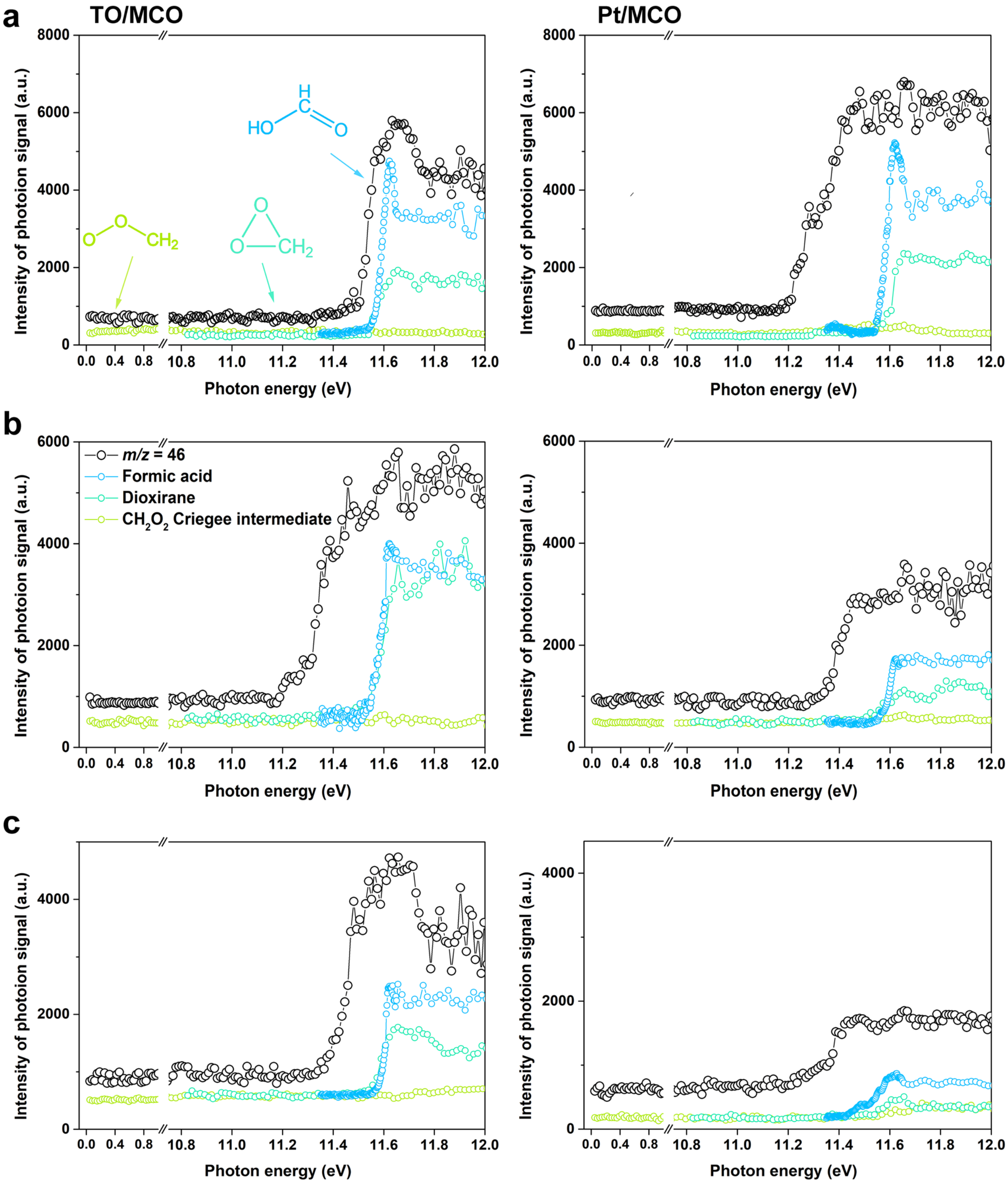

Figure 3. Determinations of the m/z = 46 species by the varying photoionization energies in the reaction of CH_2O with TO/MCO and Pt/MCO in different humid conditions at 72% (a and b), 50% (c and d), and 0.7% (e and f).

reactions with proton ions decreased the number of L-acid sites. By contrast, the XPS spectra show distinct changes in O 1s, Mn 2p, and Pt 4f peaks in Pt/MCO during the reaction. The O_{latt}/O_{ads} ratio increased from 0.17 to 0.28, and large reductions in Mn^{4+}/Mn^{3+} were found from 3.41 to 1.69. The coexistence of metallic and oxidized Pt was observed. The oxidation states of Pt were increased throughout the reaction, through which free electrons could be released to support the potential-dependent hydration structure and the electron-dependent Lewis active sites of Pt/MCO shown in Figure 1. Compared with those in TO/MCO and MCO, the binding energies (BE) of O_{latt}, O_{ads}, and Mn $2p_{3/2}$ peaks shifted to low values in Pt/MCO, indicating a strong charge exchange in metal−support interactions.[43,44] These findings demonstrate that accepting negative charges[44] on Mn and O sites from the oxidized Pt can facilitate the activation of reactive oxygen species.[45] However, the generation of more Mn^{3+} in Pt/MCO was verified by the low BE shift of Mn. Consequently, failure to maintain a high oxidation state of metal oxides affects the interfacial water structure and the M−O bridging mode.

Overall, L-acid sites play a key role in the selectivity of the cleavage of carbonyl and carboxylic species.[22,36,37] The active-

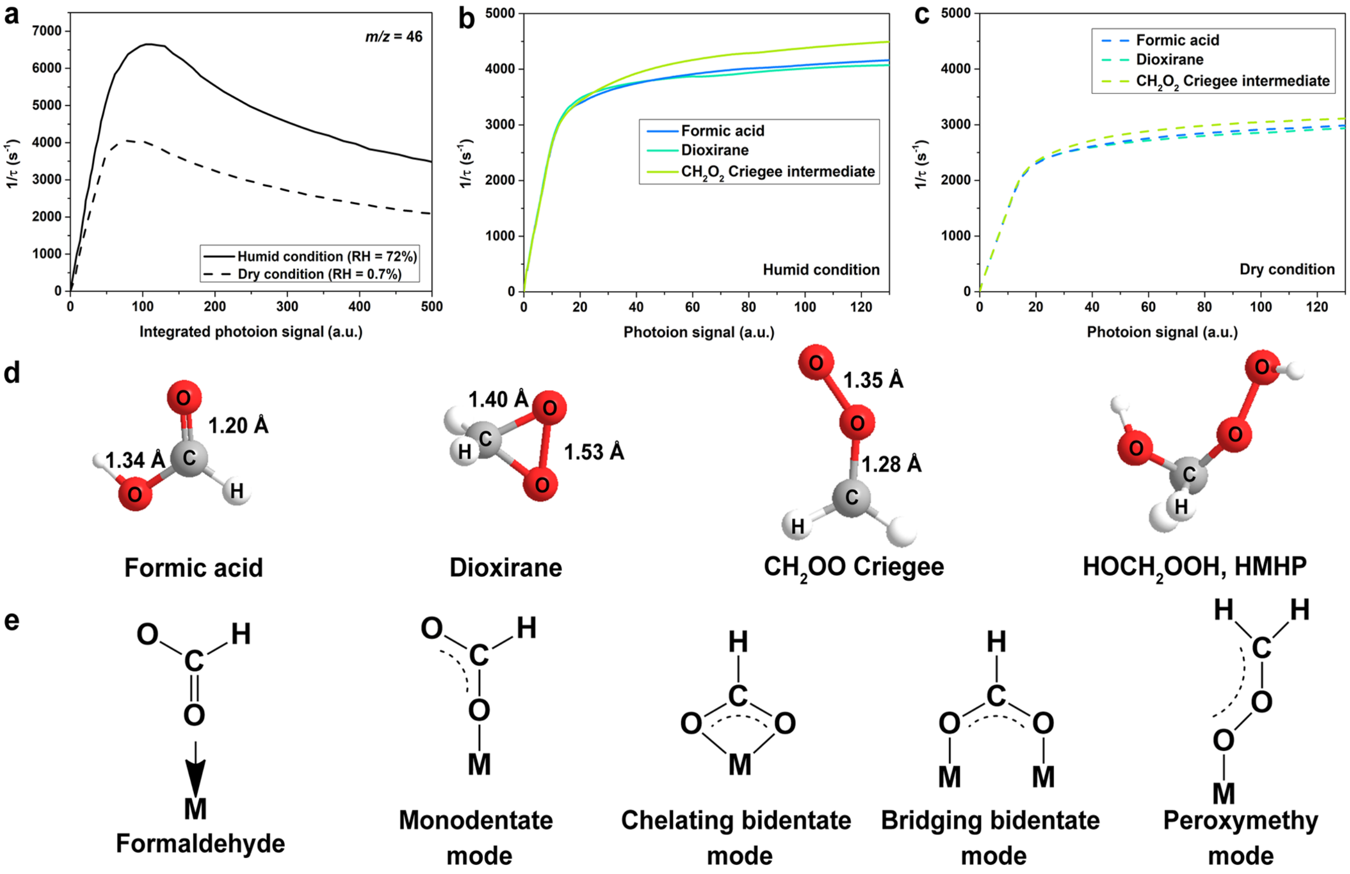

Figure 4. Decay rate (reciprocal of the lifetime τ) of the integrated photoion signal of $m/z = 46$ species (a) and comparisons in the constant decay rates of photoion signals of the three CH_2OO isomers during CH_2O oxidation with TO/MCO in humid (b) and dry conditions (c). Geometries of the three CH_2OO intermediates and the very faint byproduct HMHP, indicating the preferential occurrence of CH_2OO reactions in moisture (d). Intermediates formed under the CH_2O oxidation with the surface metal site (M) of TO/MCO by the proposed bridging modes (e).

site exposure and oxidation selectivity of the RCO catalysts under unfavorable reaction conditions can be controlled by precisely adjusting the molar ratio of metallic ions.

In Situ Measurements of CH_2OO Speciation and Kinetics. Direct measurements of CH_2OO species were performed using time-of-flight photoionization mass spectrometry in Figure 2. The millisecond resolution of the mass spectrometer is sufficient to determine the photoion signal of the CH_2OO group (mass/charge $[m/z] = 46$ peak) produced from the catalytic oxidation of CH_2O. First, the time-of-flight photoion signal of CH_2OO was carefully calibrated following the reported photoionization mass spectrometric detection of CH_2OO,[2] which was formed in the $CH_2I + O_2$ reaction after the 248 nm photolysis of CH_2I_2/O_2 (SI Figure S8). The kinetic profile of CH_2OO in the CH_2I_2/O_2 system followed the pseudo-first-order kinetic scheme as the decay rate of CH_2OO was fitted as a constant. The formation and removal of CH_2OO were well proportionate with those of precursor CH_2I. The decay of CH_2OO was independent of O_2 concentrations, suggesting that CH_2OO can be directly measured under ambient conditions. Here the CH_2OO ($m/z = 46 + 0.005$ amu) lifetime was correlated with the decay of CH_2O ($m/z = 30$) over catalysts (see Figure 2a) and calibrated from C_2H_6O ($m/z = 46 + 0.042$ amu) via time-of-flight distribution of the $m/z = 46$ signal (see Figure 2b). Very faint photoionization signal at $m/z = 64$ was assigned to HMHP. The kinetic analysis of HMHP chemistry remains uncertain and is thought to be generated from the reaction of CH_2OO with water molecules.[2,8]

In Figure 3, the photoionization spectra of the CH_2OO isomers were identified by scanning the ionizing photon energy, and impacts of moisture on the photoionization intensity of the isomers were studied in the reaction of CH_2O with TO/MCO and Pt/MCO. The signal integration of CH_2OO photoionization spectrum is roughly the integral sum of the photoion signal of the three isomeric coproducts with different photoionization energies, which were also calibrated in the CH_2I_2 ozonolysis system (SI Figure S9). Dioxirane and formic acid were identified in much higher ionization energies at 10.83 and 11.31 eV, respectively. The spectrum that originated from only 0.05 eV, which is much smaller than the theoretical predictions of 9.98 eV, was assigned to CH_2OO Criegee.[46] Moreover, CH_2OO Criegee is thought to possess some single bond characters,[2,6,27,46] which are ascribed to the rapid dissociation of C−C and O−O bonds from the ozonolysis of unsaturated hydrocarbons. This work cannot completely rule out CH_2OO Criegee given its probable involvement in side or secondary processes (e.g., HMHP production from CH_2OO reaction with H_2O or CH_2O regeneration).[2,27] The CH_2OO formations were comparable between TO/MCO and Pt/MCO at a higher RH of 72% but started to decline in Pt/MCO at lower moisture more significantly than those in TO/MCO. These observations are consistent with the higher CH_2O removal efficiencies of TO/MCO than Pt/MCO at various humidity levels (see Figure 5c

DOI: 10.1021/acs.est.8b06234
Environ. Sci. Technol. 2019, 53, 5230−5240

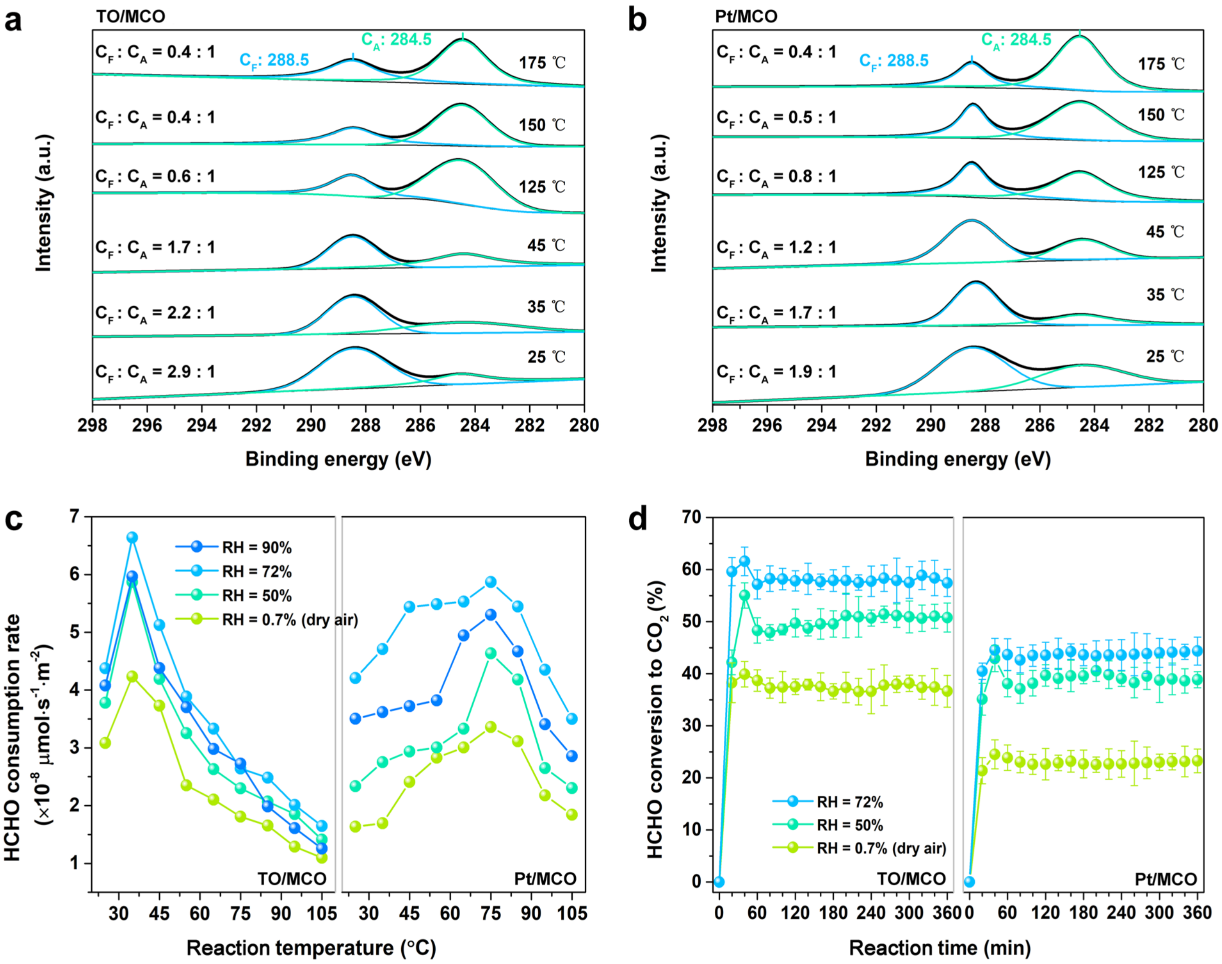

Figure 5. In situ C 1s XP spectra evolution of TO/MCO (a) and Pt/MCO (b) after CH_2O adsorption heating under Ar. Moisture-dependent CH_2O consumption rate as a function of reaction temperature (c). CH_2O conversion to CO_2 at different humidity levels during the isothermal reaction at 35 °C (d).

and d). The photoion signals of formic acid that remained the highest at various humidity levels indicate the main primary intermediate. Formations of the small dioxirane and minor CH_2OO Criegee intermediate are estimated through further thermal isomerization or dissociation from carboxylic groups (the symmetric υ_s and asymmetric stretching υ_{as} (COO)).[2,5] These results match the recently reported in situ FT−IR study, wherein the formations of δ [CH_2] corresponding to υ_s [OH] are correlated with the decay of υ_s [CH] groups.[22] Hence, compared with minor formic acid and dioxirane observed in the atmospheric oxidation,[2,5,8] main formic acid and dioxirane account for a substantial proportion in the CH_2OO group in CH_2O oxidation.

Changes in the decay rates of CH_2OO in humid and dry feeds were examined under TO/MCO. The experimental lifetime of CH_2OO was sufficiently long to allow direct kinetic measurements in the continuous reaction. The reciprocal of the lifetime (τ) of CH_2OO is denoted as the decay rate in Figure 4 and can arrive at constant within several milliseconds regardless of changes in reactant concentrations. In particular, low RH prohibits the adsorption and decomposition of CH_2O at ambient temperatures. Figure 4a shows that the decay rates of the signal integration of CH_2OO differed in humid and dry conditions. Approximately 6.6×10^3 s^{-1} of the decay rate of the CH_2OO group was attained in the humid feed, whereas the rate under TO/MCO was up to 4.0×10^3 s^{-1} in the dry feed. However, the CH_2OO removal rate was gradually slower than its formation due to the persistence of the CH_2O conversion, indicating that the CH_2OO lifetime was difficult to experimentally estimate. As anticipated, the decay rate in dry air did not largely increase and the longest CH_2OO lifetime τ was estimated up to 0.5 ms in the dry air, which is four times faster than that estimated in the literature for approximately 2 ms in tropospheric Criegee reactions.[2] The decay rates of the three CH_2OO isomers after reaching an extremely short steady state were compared in the humid and dry feeds (Figure 4b and c). Their reaction kinetics are distinct but follow the same descending order: CH_2OO Criegee intermediate, formic acid, and dioxirane. By contrast, the very minor CH_2OO Criegee intermediate has the fastest decay rate in humid (4.1×10^3 s^{-1}) and dry (2.9×10^3 s^{-1}) feeds. The RCO of CH_2O, in coordination with the production, stabilization, and removal of CH_2OO, is preferable at high humidity. In other words, the moisture-dependent decay of CH_2OO would restrict the RCO activity in practice.

In Figure 4d, a short C−O bond length (approximately 1.28 Å) and a long O−O bond (approximately 1.35 Å) of CH_2OO Criegee intermediate were observed[6,46] relative to those of formic acid and dioxirane. The rapid kinetics of the Criegee intermediate were proven in trapping experiments with its scavenger NO_2 and SO_2 under tropospheric conditions.[2,5,47] Formaldehyde conversion to formic acid and dioxirane

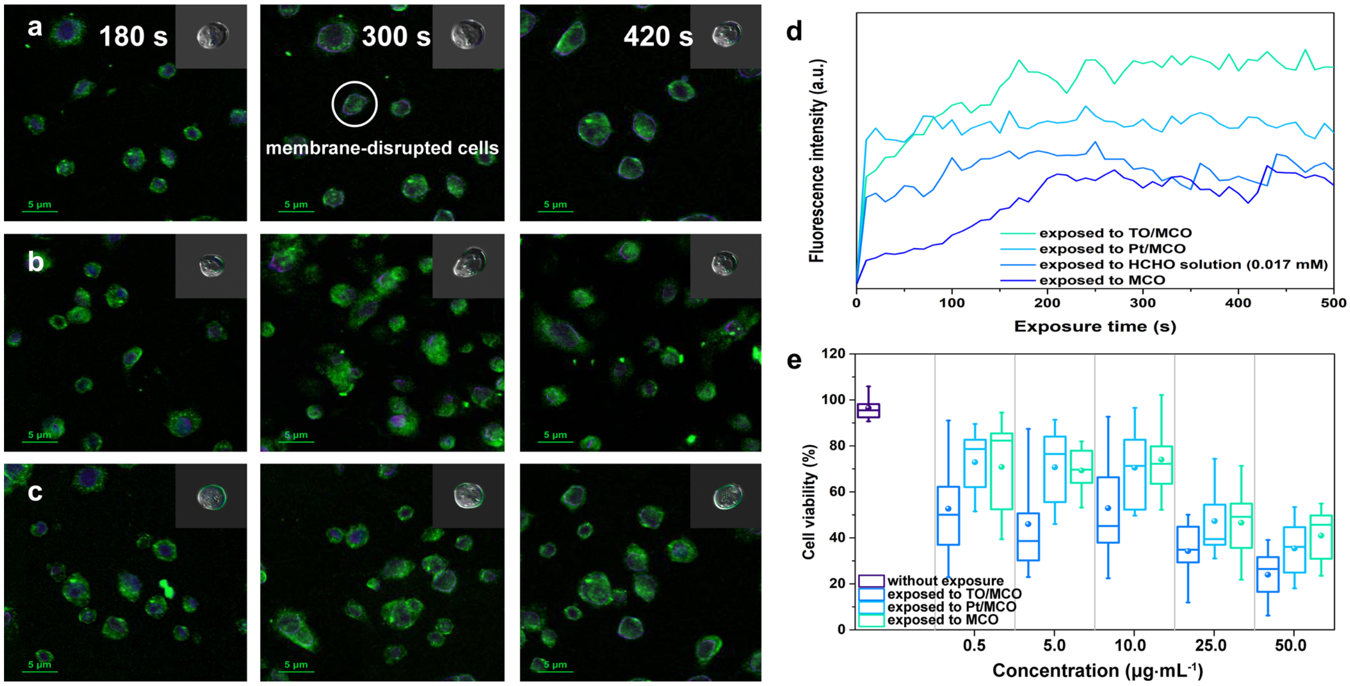

Figure 6. Time-lapse of confocal laser scanning microscope images of yeast cells exposed to spent TO/MCO (a), Pt/MCO (b), and MCO (c) NPs after CH_2O oxidation was terminated at 180, 300, and 420 s. Disrupted cells stained by PI were labeled with a purple fluorophore, with high-resolution 3D images shown in the inset. Fluorescence intensity of the disrupted cells stained by PI after exposure to the NPs and 0.017 mM CH_2O solutions (d). Comparisons of cell viability after exposure to different concentrations of the three spent NPs using the CFU counting method (e).

preferentially occurs through monodentate binding and bidentate coordination with metal sites of TO/MCO, respectively, as shown in Figure 4e. A peroxymethy bridging mode of −COO coordination with the active sites is thought to be more available for the dissociative adsorption of the weakened O−O than the strengthened C−O bond of CH_2OO Criegee intermediate.

Dioxirane has the longest lifespan and is formed possibly due to the asymmetric isomerization of carboxylic bonds.[2,6,46] Moreover, its decay rate is slightly weaker than that of formic acid, suggesting that the decomposition of dioxirane (C−O bond of approximately 1.40 Å) is more refractory than that of formic acid (C═O bond of approximately 1.20 Å). If the O−H bond dissociation of hydroxyl and carboxylic bonds is sufficiently activated on the metal sites of catalysts, then the remaining carboxylic groups would be bridged to the epidioxyl groups of dioxirane under the electrophilic behavior of oxygen atoms.[48] Given that almost no reactions exist between epidioxyl and carboxylic groups at room temperature, dioxirane is more inactive in the catalytic oxidation than the two other intermediates. The formation and decay of CH_2OO Criegee are rather complex and remain unclear. CH_2OO Criegee is thought to possess some single bond characters,[2,6,27,46] which are assumed to rapidly dissociate into C−C and O−O bonds from the oxidation of unsaturated hydrocarbons. Furthermore, the linear relation between CH_2O disappearance and CH_2OO formation is not fully understood,[2,3] in which small amounts of formaldehyde may be regenerated in reactions of the O atom with CH_2OO Criegee intermediate. Consequently, preserving a large accumulation of CH_2OO on the surface of catalysts, such as dioxirane and formic acid which are more resistant to decomposition than CH_2O, is challenging to the complete catalytic oxidation of CH_2O.

CH_2O Adsorption and Complete Oxidation Enhancement. The RCO of CH_2O facilitates adsorption and favors high humidity. In this reaction, the initial physioadsorption relies on the improved specific surface areas and porosity followed by the chemisorption involving H bonding of methyl groups to interfacial water molecules[16,23] and O atom bridging of carbonyl and carboxylic groups onto surface metal sites.[22,26,48] In situ C 1s XPS studies as a function of reaction temperature were compared between the CH_2O-exposed TO/MCO and Pt/MCO (see Figure 5a and b). The broad photopeak at 288.5 eV was assigned to the presence of formaldehyde/mono(bi)-dentate formate species (C_F), and the photopeak at low BE (284.5 eV) was assigned to adventitious carbon (C_A).[19,26] As temperature increased from 25 to 45 °C, the ratios of C_F to C_A photopeak areas in Pt/MCO were all lower than those in TO/MCO. Better CH_2O/formate adsorption and oxidation were found at the surface of TO/MCO at ambient temperatures, consistent with the corresponding catalytic activities illustrated in Figure 5c and d. The adverse effects on the C_F intensity were apparent when temperature exceeded 45 °C. Above 125 °C, the decreases in C_F photopeak were larger in TO/MCO than in Pt/MCO, indicating that the noble−metallic activity is preferential at increased temperatures.[49,50] C_A photopeak became precipitous at 125 °C−175 °C whereas weak CH_2O and formate signals were found in the C_F photopeak, which are indicative of CO oxidation and CO_2 yield in favor of this temperature range.[10,19] The catalytic activity for the CH_2O removal was evaluated using the turnover frequencies (TOFs) per unit of surface area ($mol_{HCHO} \cdot s^{-1} \cdot m_{cat}^{-2}$), defined as the ratio of the reaction rate to the active-site density of catalysts. The variations in the CH_2O consumption rates with reaction temperatures were found over TO/MCO, Pt/MCO, and MCO at different humidity levels in Figure 5c and SI Figure S10a. The increased

DOI: 10.1021/acs.est.8b06234
Environ. Sci. Technol. 2019, 53, 5230−5240

moisture in the feed promoted CH_2O oxidation, but excessively high RH restricted this reaction. The rate of TO/MCO decreased as temperature increased after the maximum of 6.6×10^{-8} $\mu mol_{HCHO} \cdot s^{-1} \cdot m_{cat}^{-2}$ was obtained at 35 °C. By contrast, the loading fabrication of Pt on the MCO surface resulted in the highest rate obtained at above 70 °C, consistent with the in situ XPS results. Notably, when moisture decreased under the low-temperature range of 25−45 °C, the consumption rates of TO/MCO were remediated because of its hydrophilic interface, approximately 30% higher than those of Pt/MCO and an order of magnitude higher than MCO. Hence, the TOFs of TO/MCO in the CH_2O oxidation were much higher than those of Pt/MCO in the dry feed at low temperatures. The CH_2O conversion efficiencies to CO_2 were proportional to the TOFs under the identical test conditions and were reduced with decreased moisture at a constant reaction temperature in Figure 5d and SI Figure S10b. The conversion rate of TO/MCO remained at 40.5% in the entire test, whereas large decreases (average of 22.6%) were found for Pt/MCO in dry air. Aside from the insufficient CO oxidation at low temperatures, the catalytic oxidation of Pt/MCO is flagging, indicative of deactivation occurred.[10,18,20]

Aside from the better BET performance, strong adsorption of CH_2O and CH_2OO intermediates can be initiated in dry air by the association of the H bond of alpha-methyl groups with the hydroxyl molecules in the well-defined water interfaces of TO/MCO (see Figure 1a and b). In the subsequent decomposition of the ad-carboxylic (HO—C═O) groups, the O−H bond dissociation was likely stimulated at active sites on metal oxides.[48] Although the formation of C−O from the C═O oxidation was triggered by the activation of reactive oxygen species at the identical active sites,[22] the pathway was somewhat uncertain because of the complexity of bond characters in the production of dioxirane and CH_2OO Criegee. To date, the correlations between the active sites and formation of the CH_2OO isomers are difficult to ascertain because the laboratory measurements of the quantitative effects of active sites on the production and decay of intermediates cannot be directly carried out. Overall, exploring an ordered array of water/TiO_2 interface of catalysts is believed to help the routine catalyst supports enhance the complete adsorption and conversion of CH_2OO to CO_2 under unfavorable reaction moistures and temperatures.

Cytotoxicological Assessment of CH_2OO Intermediates. CH_2O is already recognized as a common environmental toxin even at low concentrations and has been long associated with the initiation and progression of diseases of the upper respiratory tract and several types of severe cancers.[10,28,29] To date, the toxicological potency of emissions from CH_2OO intermediates has not yet been studied due to their uncertain speciation and millisecond lifetime. Given that the cellular structure and organism function of yeast have many similarities with cells in plants and animals,[51,52] the cytotoxicity of the spent catalyst NPs (after the reaction was terminated at three given timeslots) exposed to yeast cells was evaluated relative to the fresh NPs and formaldehyde in Figure 6. As shown in Figure 6a−c, all cells stained by DAPI were labeled with green fluorophore and those with disrupted membrane stained by PI were labeled with purple fluorophore in the FCSM images. After an initial 180 s reaction, the spent TO/MCO and Pt/MCO NPs in the FCSM images of the cell viability were observed to induce more apparent purple illuminations than those in MCO NPs, which were examined with the benign cell viability of their fresh NPs[22] (see also SI Figure S11). Similarly, more purple fluorophores were highlighted under exposure to the spent catalysts after the prolonged reactions in 420 s. Hence, the cell membrane and cytoplasmic area were disrupted when the spent NPs adhered to or were transported into the yeast cells.

As shown in Figure 6d, the fluorescence intensities of the cell-exposed spent NPs stained by PI were investigated to evaluate the cytotoxicity of the CH_2OO intermediates compared with those of cell exposure to a 0.017 mM CH_2O aqueous solution (approximately 500 ppb of the initial gaseous CH_2O concentrations in the reaction). Interestingly, the PI fluorescence intensity of TO/MCO NPs inside the cell was more intense than that of Pt/MCO NPs, even more than that of CH_2O. Corresponding to large amounts of the generated CH_2OO intermediates at TO/MCO (see Figure 3), possible toxin species apart from formic acid were assumed to include the dioxirane and CH_2OO Criegee, resulting in more cell disruption and death.

The number of CFUs of living yeast cells[53] was counted to double check the distinct cytotoxicity of the CH_2OO intermediates in Figure 6e. The yeast cells were exposed to the spent NPs with different concentrations of 0.5, 5, 10, 25, 50, and 100 $\mu g \cdot mL^{-1}$ dispersed in 5 mM aqueous NaCl solutions. The number of CFUs on the yeast-NP plate was compared with that of CFUs on the control plate, which did not include NPs. All cell viabilities weakened with the increase in concentrations of NPs. Similarly, the spent Pt/MCO and MCO NPs stimulated more cell proliferation and were less lethal than the spent TO/MCO NPs. An average of 50% cell death occurred at 0.5 $\mu g \cdot mL^{-1}$ NP concentration, and up to 80% cell death was observed after exposure to 50 $\mu g \cdot mL^{-1}$ of TO/MCO NPs. Therefore, much larger amounts of CH_2O and CH_2OO intermediates can be adsorbed at the TO/MCO surface, thereby providing a basis for the complete conversion of CH_2O to CO_2 and suppressing toxic intermediate emissions to ambient conditions. This work also stimulates future study on the rational design and selectivity enhancement of reliable catalysts for practical applications under different ambient conditions.

■ ASSOCIATED CONTENT

Ⓢ Supporting Information

The Supporting Information is available free of charge on the ACS Publications website at DOI: 10.1021/acs.est.8b06234.

> Preparations of the precursor MCO and TO/MCO catalysts; Fitted equation of SFG intensity; Schematic diagrams of SFG spectrometry and time-of-flight tunable synchrotron photoionization mass spectrometry; Voltammograms of TO/MCO and Pt/MCO in the SFG spectroelectrochemical measurements; Characterizations of XRD, TEM, BET, and XPS for as-prepared catalysts; Calibration of the time-of-flight photoion signal of m/z = 46 products; Calibration of the photoionization spectra of CH_2OO by the varying photoionization energies; Catalytic activity of precursor MCO; Yeast cell viability observed by FCSM imaging after exposure to the fresh catalysts (PDF)

■ AUTHOR INFORMATION

Corresponding Authors

*(S.-c.L.) E-mail: ceslee@polyu.edu.hk.

*(W.H.) E-mail: keithho@eduhk.hk.

ORCID

Haiwei Li: 0000-0003-4632-7490

Yu Huang: 0000-0003-3334-4849

Shun-cheng Lee: 0000-0001-5144-8372

Notes

The authors declare no competing financial interest.

■ ACKNOWLEDGMENTS

This work was supported by the National Key Research and Development Program of China (2016YFA0203000), the Research Grants Council of Hong Kong Government (Project No. T24/504/17, PolyU152083/14E, PolyU152090/15E, and GRF 18301117), the Hong Kong RGC Collaborative Research Fund (C5022-14G), and the Dean's Reserved Fund, FLASS (04360) and IRG (R4016) from EdUHK.

■ REFERENCES

(1) Johnson, D.; Marston, G. The gas-phase ozonolysis of unsaturated volatile organic compounds in the troposphere. *Chem. Soc. Rev.* **2008**, *37* (4), 699−716.

(2) Welz, O.; Savee, J. D.; Osborn, D. L.; Vasu, S. S.; Percival, C. J.; Shallcross, D. E.; Taatjes, C. A. Direct kinetic measurements of Criegee intermediate (CH_2OO) formed by reaction of CH_2I with O_2. *Science* **2012**, *335* (6065), 204−207.

(3) Taatjes, C. A.; Welz, O.; Eskola, A. J.; Savee, J. D.; Scheer, A. M.; Shallcross, D. E.; Rotavera, B.; Lee, E. P.; Dyke, J. M.; Mok, D. K. Direct measurements of conformer-dependent reactivity of the Criegee intermediate CH_3CHOO. *Science* **2013**, *340* (6129), 177−180.

(4) Welz, O.; Eskola, A. J.; Sheps, L.; Rotavera, B.; Savee, J. D.; Scheer, A. M.; Osborn, D. L.; Lowe, D.; Murray Booth, A.; Xiao, P. Rate coefficients of C1 and C2 Criegee intermediate reactions with formic and acetic acid near the collision limit: direct kinetics measurements and atmospheric implications. *Angew. Chem., Int. Ed.* **2014**, *53* (18), 4547−4550.

(5) Chao, W.; Hsieh, J.-T.; Chang, C.-H. Direct kinetic measurement of the reaction of the simplest Criegee intermediate with water vapor. *Science* **2015**, *347* (6223), 751−754.

(6) Su, Y.-T.; Huang, Y.-H.; Witek, H. A.; Lee, Y.-P. Infrared absorption spectrum of the simplest Criegee intermediate CH_2OO. *Science* **2013**, *340* (6129), 174−176.

(7) Chen, L.; Huang, Y.; Xue, Y.; Cao, J.; Wang, W. Competition between HO_2 and H_2O_2 reactions with CH_2OO/anti-CH_3CHOO in the oligomer formation: a theoretical perspective. *J. Phys. Chem. A* **2017**, *121* (37), 6981−6991.

(8) Su, Y.-T.; Lin, H.-Y.; Putikam, R.; Matsui, H.; Lin, M.; Lee, Y.-P. Extremely rapid self-reaction of the simplest Criegee intermediate CH_2OO and its implications in atmospheric chemistry. *Nat. Chem.* **2014**, *6* (6), 477−483.

(9) Donahue, N. M.; Drozd, G. T.; Epstein, S. A.; Presto, A. A.; Kroll, J. H. Adventures in ozoneland: down the rabbit-hole. *Phys. Chem. Chem. Phys.* **2011**, *13* (23), 10848−10857.

(10) Quiroz Torres, J.; Royer, S.; Bellat, J. P.; Giraudon, J. M.; Lamonier, J. F. Formaldehyde: catalytic oxidation as a promising soft way of elimination. *ChemSusChem* **2013**, *6* (4), 578−592.

(11) Huang, H.; Xu, Y.; Feng, Q.; Leung, D. Y. Low temperature catalytic oxidation of volatile organic compounds: a review. *Catal. Sci. Technol.* **2015**, *5* (5), 2649−2669.

(12) Nie, L.; Yu, J.; Jaroniec, M.; Tao, F. F. Room-temperature catalytic oxidation of formaldehyde on catalysts. *Catal. Sci. Technol.* **2016**, *6* (11), 3649−3669.

(13) Xu, H.; Yan, N.; Qu, Z.; Liu, W.; Mei, J.; Huang, W.; Zhao, S. Gaseous heterogeneous catalytic reactions over Mn-based oxides for environmental applications: a critical review. *Environ. Sci. Technol.* **2017**, *51* (16), 8879−8892.

(14) Miao, L.; Wang, J.; Zhang, P. Review on manganese dioxide for catalytic oxidation of airborne formaldehyde. *Appl. Surf. Sci.* **2019**, *466*, 441−453.

(15) Guo, J.; Lin, C.; Jiang, C.; Zhang, P. Review on noble metal-based catalysts for formaldehyde oxidation at room temperature. *Appl. Surf. Sci.* **2019**, *475*, 237−255.

(16) Wang, J.; Zhang, P.; Li, J.; Jiang, C.; Yunus, R.; Kim, J. Room-temperature oxidation of formaldehyde by layered manganese oxide: effect of water. *Environ. Sci. Technol.* **2015**, *49* (20), 12372−12379.

(17) Kwon, D. W.; Seo, P. W.; Kim, G. J.; Hong, S. C. Characteristics of the HCHO oxidation reaction over Pt/TiO_2 catalysts at room temperature: the effect of relative humidity on catalytic activity. *Appl. Catal., B* **2015**, *163*, 436−443.

(18) Wang, Y.; Zhu, X.; Crocker, M.; Chen, B.; Shi, C. A comparative study of the catalytic oxidation of HCHO and CO over $Mn_{0.75}Co_{2.25}O_4$ catalyst: the effect of moisture. *Appl. Catal., B* **2014**, *160*, 542−551.

(19) Quiroz, J.; Giraudon, J. M.; Gervasini, A.; Dujardin, C.; Lancelot, C.; Trentesaux, M.; Lamonier, J. F. Total oxidation of formaldehyde over MnO_x-CeO_2 catalysts: the effect of acid treatment. *ACS Catal.* **2015**, *5*, 2260−2269.

(20) Tang, X.; Chen, J.; Huang, X.; Xu, Y.; Shen, W. Pt/MnO_x-CeO_2 catalysts for the complete oxidation of formaldehyde at ambient temperature. *Appl. Catal., B* **2008**, *81* (1), 115−121.

(21) Han, X.; Li, C.; Liu, X.; Xia, Q.; Wang, Y. Selective oxidation of 5-hydroxymethylfurfural to 2,5-furandicarboxylic acid over MnO_x-CeO_2 composite catalysts. *Green Chem.* **2017**, *19* (4), 996−1004.

(22) Li, H.; Huang, T.; Lu, Y.; Cui, L.; Wang, Z.; Zhang, C.; Lee, S.; Huang, Y.; Cao, J.; Ho, W. Unraveling the mechanisms of room-temperature catalytic degradation of indoor formaldehyde and its biocompatibility on colloidal TiO_2-supported MnO_x-CeO_2. *Environ. Sci.: Nano* **2018**, *5* (5), 1130−1139.

(23) Hussain, H.; Tocci, G.; Woolcot, T.; Torrelles, X.; Pang, C.; Humphrey, D.; Yim, C.; Grinter, D.; Cabailh, G.; Bikondoa, O. Structure of a model TiO_2 photocatalytic interface. *Nat. Mater.* **2017**, *16* (4), 461−466.

(24) Banerjee, S.; Dionysiou, D. D.; Pillai, S. C. Self-cleaning applications of TiO_2 by photo-induced hydrophilicity and photocatalysis. *Appl. Catal., B* **2015**, *176*, 396−428.

(25) Lu, Y. Self-hydrogenated shell promoting photocatalytic H_2 evolution on anatase TiO_2. *Nat. Commun.* **2018**, *9* (1), 2752−2760.

(26) Selvakumar, S.; Nuns, N.; Trentesaux, M.; Batra, V.; Giraudon, J.-M.; Lamonier, J.-F. Reaction of formaldehyde over birnessite catalyst: a combined XPS and ToF-SIMS study. *Appl. Catal., B* **2018**, *223*, 192−200.

(27) Hasson, A. S.; Chung, M. Y.; Kuwata, K. T.; Converse, A. D.; Krohn, D.; Paulson, S. E. Reaction of Criegee Intermediates with water vapor an additional source of OH radicals in alkene ozonolysis? *J. Phys. Chem. A* **2003**, *107* (32), 6176−6182.

(28) Salthammer, T.; Mentese, S.; Marutzky, R. Formaldehyde in the indoor environment. *Chem. Rev.* **2010**, *110* (4), 2536−2572.

(29) Brewer, T. F.; Burgos-Barragan, G.; Wit, N.; Patel, K. J.; Chang, C. J. A 2-aza-cope reactivity-based platform for ratiometric fluorescence imaging of formaldehyde in living cells. *Chem. Sci.* **2017**, *8* (5), 4073−4081.

(30) Burgos-Barragan, G.; Wit, N.; Meiser, J.; Dingler, F. A.; Pietzke, M.; Mulderrig, L.; Pontel, L. B.; Rosado, I. V.; Brewer, T. F.; Cordell, R. L. Mammals divert endogenous genotoxic formaldehyde into one-carbon metabolism. *Nature* **2017**, *548* (7669), 549−554.

(31) Huang, Y.; Wang, P.; Wang, Z.; Rao, Y.; Cao, J.-j.; Pu, S.; Ho, W.; Lee, S. C. Protonated $g-C_3N_4/Ti^{3+}$ self-doped TiO_2 nanocomposite films: room-temperature preparation, hydrophilicity, and application for photocatalytic NO_x removal. *Appl. Catal., B* **2019**, *240*, 122−131.

(32) Noguchi, H.; Okada, T.; Uosaki, K. SFG study on potential-dependent structure of water at Pt electrode/electrolyte solution interface. *Electrochim. Acta* **2008**, *53* (23), 6841−6844.

(33) Noguchi, H.; Okada, T.; Uosaki, K. Molecular structure at electrode/electrolyte solution interfaces related to electrocatalysis. *Faraday Discuss.* **2009**, *140*, 125−137.

(34) Ferreira de Morais, R.; Franco, A. A.; Sautet, P.; Loffreda, D. Interplay between reaction mechanism and hydroxyl species for water formation on Pt (111). *ACS Catal.* **2015**, *5* (2), 1068−1077.

(35) Zugic, B.; Wang, L.; Heine, C.; Zakharov, D. N.; Lechner, B. A.; Stach, E. A.; Biener, J.; Salmeron, M.; Madix, R. J.; Friend, C. M. Dynamic restructuring drives catalytic activity on nanoporous gold-silver alloy catalysts. *Nat. Mater.* **2017**, *16* (5), 558−564.

(36) Weng, X.; Sun, P.; Long, Y.; Meng, Q.; Wu, Z. Catalytic oxidation of chlorobenzene over $Mn_xCe_{1-x}O_2$/HZSM-5 catalysts: a study with practical implications. *Environ. Sci. Technol.* **2017**, *51* (14), 8057−8066.

(37) Wang, J.; Wang, X.; Liu, X.; Zhu, T.; Guo, Y.; Qi, H. Catalytic oxidation of chlorinated benzenes over V_2O_5/TiO_2 catalysts: the effects of chlorine substituents. *Catal. Today* **2015**, *241*, 92−99.

(38) Van de Vyver, S.; Odermatt, C.; Romero, K.; Prasomsri, T.; Román-Leshkov, Y. Solid Lewis acids catalyze the carbon-carbon coupling between carbohydrates and formaldehyde. *ACS Catal.* **2015**, *5* (2), 972−977.

(39) Yarulina, I.; Wispelaere, K. D.; Bailleul, S.; Goetze, J.; Radersma, M.; Abouhamad, E.; Vollmer, I.; Goesten, M.; Mezari, B.; Hensen, E. J. M. Structure-performance descriptors and the role of Lewis acidity in the methanol-to-propylene process. *Nat. Chem.* **2018**, *10*, 804−812.

(40) Albonetti, S.; Blasioli, S.; Bonelli, R.; Mengou, J. E.; Scirè, S.; Trifirò, F. The role of acidity in the decomposition of 1,2-dichlorobenzene over TiO_2-based V_2O_5/WO_3 catalysts. *Appl. Catal., A* **2008**, *341* (1−2), 18−25.

(41) Feng, X.; Sayle, D. C.; Wang, Z. L.; Paras, M. S.; Santora, B.; Sutorik, A. C.; Sayle, T. X.; Yang, Y.; Ding, Y.; Wang, X. Converting ceria polyhedral nanoparticles into single-crystal nanospheres. *Science* **2006**, *312* (5779), 1504−1508.

(42) Zhang, C.; Michaelides, A.; King, D. A.; Jenkins, S. J. Anchoring sites for initial Au nucleation on CeO_2(111): O vacancy versus Ce vacancy. *J. Phys. Chem. C* **2009**, *113* (16), 6411−6417.

(43) Yan, Z. X.; Zhihua; Yu, J.; Jaroniec, M. Highly active mesoporous ferrihydrite supported catalyst for formaldehyde removal at room temperature. *Environ. Sci. Technol.* **2015**, *49* (11), 6637−6644.

(44) Duan, B.; Yang, J.; Salvador, J. R.; He, Y.; Zhao, B.; Wang, S.; Wei, P.; Ohuchi, F. S.; Zhang, W.; Hermann, R. P. Electronegative guests in $CoSb_3$. *Energy Environ. Sci.* **2016**, *9* (6), 2090−2098.

(45) Lu, Y.; Huang, Y.; Zhang, Y.; Cao, J.-j.; Li, H.; Bian, C.; Lee, S. C. Oxygen vacancy engineering of $Bi_2O_3/Bi_2O_2CO_3$ heterojunctions: Implications of the interfacial charge transfer, NO adsorption and removal. *Appl. Catal., B* **2018**, *231*, 357−367.

(46) Nguyen, M. T.; Nguyen, T. L.; Ngan, V. T.; Nguyen, H. M. T. Heats of formation of the Criegee formaldehyde oxide and dioxirane. *Chem. Phys. Lett.* **2007**, *448* (4), 183−188.

(47) Vereecken, L.; Harder, H.; Novelli, A. The reaction of Criegee intermediates with NO, RO_2, and SO_2, and their fate in the atmosphere. *Phys. Chem. Chem. Phys.* **2012**, *14* (42), 14682−14695.

(48) Jia, X.; Ma, J.; Xia, F.; Xu, Y.; Gao, J.; Xu, J. Carboxylic acid-modified metal oxide catalyst for selectivity-tunable aerobic ammoxidation. *Nat. Commun.* **2018**, *9* (1), 933−939.

(49) Zhang, C.; Li, Y.; Wang, Y.; He, H. Sodium-promoted Pd/TiO_2 for catalytic oxidation of formaldehyde at ambient temperature. *Environ. Sci. Technol.* **2014**, *48* (10), 5816−5822.

(50) Chen, B.-b.; Zhu, X.-b.; Crocker, M.; Wang, Y.; Shi, C. FeO_x-supported gold catalysts for catalytic removal of formaldehyde at room temperature. *Appl. Catal., B* **2014**, *154*, 73−81.

(51) Nomura, T.; Miyazaki, J.; Miyamoto, A.; Kuriyama, Y.; Tokumoto, H.; Konishi, Y. Exposure of the yeast Saccharomyces cerevisiae to functionalized polystyrene latex nanoparticles: influence of surface charge on toxicity. *Environ. Sci. Technol.* **2013**, *47* (7), 3417−3423.

(52) Eigenheer, R.; Castellanos, E. R.; Nakamoto, M. Y.; Gerner, K. T.; Lampe, A. M.; Wheeler, K. E. Silver nanoparticle protein corona composition compared across engineered particle properties and environmentally relevant reaction conditions. *Environ. Sci.: Nano* **2014**, *1* (3), 238−247.

(53) Huang, Y.; Liang, Y.; Rao, Y.; Zhu, D.; Cao, J.-j.; Shen, Z.; Ho, W.; Lee, S. C. Environment-friendly carbon quantum dots/$ZnFe_2O_4$ photocatalysts: characterization, biocompatibility, and mechanisms for NO removal. *Environ. Sci. Technol.* **2017**, *51* (5), 2924−2933.

DOI: 10.1021/acs.est.8b06234
Environ. Sci. Technol. 2019, 53, 5230−5240